Chemical Science

ROYAL SOCIETY OF CHEMISTRY

EDGE ARTICLE

View Article Online
View Journal | View Issue

Cite this: *Chem. Sci.*, 2025, **16**, 23174

All publication charges for this article have been paid for by the Royal Society of Chemistry

Received 12th July 2025
Accepted 25th October 2025

DOI: 10.1039/d5sc05194k

rsc.li/chemical-science

AM-C33: an altermagnetic carbon

Mingqing Liao, *[a] Yuehua Wang,[a] Pengcheng Ye,[a] Chenggang Wu,[a] Haoxin Jiang,[a] Fei Zhou,[b] Jintong Guan [c] and Fengjiang Wang*[a]

Altermagnetic materials have recently garnered significant attention due to their combined advantages of spin-splitting characteristics inherent to ferromagnets and the zero-net-moment stability of antiferromagnets. p-electron spintronic materials intrinsically exhibit long-distance spin coherence and long spin lifetimes. However, to date, no theoretical or experimental realization of three-dimensional p-electron altermagnets has been reported. Herein, using first-principles calculations, we proposed a fully carbon-based p-electron altermagnetic semiconductor, denoted as AM-C33, featuring a bandgap of 0.52 eV, spin-splitting energy of 0.31 eV, and transition temperature of 121.5 K. The altermagnetic behavior arises from the tetrahedrally distributed spin atoms, in which the opposite-spin sublattices are connected by a four-fold inversion axis. In addition, strain engineering enables tuning of both the bandgap and spin-splitting magnitudes while preserving its altermagnetic order. Furthermore, this material hosts metastable phases exhibiting distinct functionalities, including a half-metal ferromagnetic state and a bipolar magnetic semiconductor ferrimagnetic state. Hence, the present work presents great promise for designing p-electron altermagnets, particularly advancing carbon-based altermagnetic materials for spintronic applications.

1. Introduction

In the modern information age, with the continued scaling down of semiconductor fabrication technology, traditional memory chips reach their bottlenecks. Owing to showing the features of fast read/write speed, high storage density, and non-volatility, magnetic random-access memory (MRAM) stands as one of the most promising memory solutions in the post-Moore era.[1,2] Over the past few decades, numerous spintronic materials have been developed, ranging from 3D to 2D structures[3,4] and covering ferromagnetic (FM) to antiferromagnetic (AFM) phases.[1,5] Traditional MRAMs mainly consist of FM materials, which are easy to control owing to spin splitting. However, FM materials suffer from inherent limitations, such as stray magnetic fields and low resonance frequencies (GHz).[6] Owing to the zero net magnetic moment, AFM (especially collinear AFM) materials exhibit inherent immunity to external magnetic perturbations and vanishing stray fields and attain resonance frequencies in the THz regime.[7] However, the persistent spin degeneracy throughout the Brillouin zone in conventional antiferromagnets—arising from time-reversal symmetry protection—leads to the absence of non-reciprocal transport effects, thereby crippling both electrical manipulation and magnetometry-based readout.[8] Recently, the newly discovered altermagnetism (AM) bridged the gap between ferro- and antiferro-magnetism, hosting spin-split bands protected by crystal symmetries yet preserving vanishing macroscopic magnetization.[8–10]

AM has attracted significant interest in recent years, spanning fundamental investigations into its symmetry analysis,[11] transport properties,[12] detection methodologies,[13,14] and high-throughput screening of novel materials.[15] Within the past few years, over 300 AM materials have been identified.[16] All the known AM materials contain heavy metal elements ($Z > 20$), which provide magnetic moment through d and f electrons. In spintronic materials, p-electron-induced systems exhibit some superior performance, such as extremely weak spin–orbit coupling (SOC), thus enabling long-distance spin transport, long electron spin coherence time, and prolonged spin lifetimes.[2,17,18] In addition, these systems serve as an ideal material for investigating spin splitting mechanisms in AM materials without interference from SOC. However, to date, no experimental or theoretical evidence has been reported for three-dimensional p-electron-induced AM.[16]

In p-electron light element systems, due to their diverse bonding configurations (sp, sp^2, and sp^3 hybridization), carbon materials demonstrate extraordinary functional properties. However, for spintronic materials, carbon presents a fundamental limitation: its intrinsic non-magnetic nature. Over the

[a]School of Materials Science and Engineering, Jiangsu University of Science and Technology, Zhenjiang 212100, China. E-mail: mingqing_liao@just.edu.cn; fjwang@just.edu.cn

[b]State Key Laboratory for Environment-friendly Energy Materials, School of Materials and Chemistry, Southwest University of Science and Technology, Mianyang, 621010, China

[c]School of Materials Science and Engineering, Jiangsu University, Zhenjiang 212013, China

past decades, significant efforts have been devoted to inducing magnetism in carbon. In 1991, magnetism was observed in tetrakis(dimethylamino)ethylene-C_{60} materials.[19] Then Makarova *et al.*[20] reported magnetism in pure one-dimensional C_{60}, which was subsequently attributed to metallic impurities. In pure carbon, magnetism is mainly shown in 2D systems (*e.g.*, twisted bilayer graphene[21]) and 3D amorphous carbon (*e.g.*, Q-carbon[22]), in which magnetism is mainly contributed from the sp^2-like threefold coordinated carbon atoms.[23] In addition, the diamond with vacancies[24] and HM-C21 (ref. 25) are theoretically proven to be magnetic. However, the AM carbon has not been reported, and the most closely related systems are other light element (*e.g.*, H, B, N, P, and S) modified 2D systems[26,27] and p-electron-induced 2D metal–organic frameworks (MOFs).[28–30]

In the present work, we proposed a new 3D carbon allotrope, denoted as AM-C33, and systematically investigated its different magnetic states. The interesting thing is that AM-C33 exhibits an AM ground state, the spin-splitting energy of which is tunable using strain engineering.

2. Computational methods

In this work, RG^2 software[31] is used to generate the structure of the new magnetic carbon allotrope, and it also assists in the discovery of several other novel carbon allotropes.[32,33] Density functional theory (DFT) calculations are performed using DS-PAW software integrated into the Device Studio program.[34,35] The exchange-correlation is described by the Perdew–Burke–Ernzerhof (PBE) functional within the generalized gradient approximation (GGA).[36] The projector augmented-wave (PAW) pseudopotential[34] with a cut-off energy of 570 eV is adopted to describe the electron–ion interaction, and $2s^22p^2$ is treated as involving valence electrons. The *k*-points are generated by specifying the grid mesh of $10 \times 10 \times 10$ using the Monkhorst–Pack method.[37] DFT + *U* with $U_{eff} = 8.6$ eV, which is determined according to Cococcioni's[38] method (Fig. S1), is applied to calculate the band structure and density of states (DOS). The convergence criteria for the self-consistent field (SCF) and full relaxation are 10^{-6} eV and 10^{-5} eV, respectively. The phonon spectrum is evaluated using density functional perturbation theory (DFPT).[39] *Ab initio* molecular dynamics (AIMD) are performed for 3000 steps with 1 fs per step at 300 K using the *NPT* ensemble, and a $2 \times 2 \times 2$ supercell with 264 atoms is used in AIMD. The elastic constants are calculated with the help of Elastic3rd,[40,41] and the mechanical stability and polycrystalline elastic constants are evaluated using the ElasticPOST code.[42] The Heisenberg model is employed to evaluate the transition temperature. The Heisenberg exchange parameters are calculated with the help of TB2J[43] and ABACUS,[44,45] and the transition temperature is determined *via* Monte Carlo simulation[46] performed on a $20 \times 20 \times 20$ supercell, as implemented in the Vampire package.[47]

3. Results and discussion

The new carbon phase with a space group of P-43M (No. 215) is presented in Fig. 1. In the unit cell, there are 33 atoms (here, we name it AM-C33) which belong to 5 different Wyckoff positions: 1*b*(0.5, 0.5, 0.5) (C1, pink in Fig. 1), 4*e*(0.6385, 0. 6385, 0. 6385) (C2, blue in Fig. 1), 4*e*(0.2801, 0. 2801, 0. 2801) (C3, red in Fig. 1), 12*i*(0.2186, 0.2186, 0.4878) (C4, green in Fig. 1), and 12*h*(0.3227, 0.5, 0) (C5, gray in Fig. 1). Except for C3, which is sp^2-hybridized, all other atoms are sp^3-hybridized. The angle of C4–C3–C4 is about 115.4°, which is close to 120°. The comparison between the current structure and the Samara Carbon Allotrope Database (SACADA),[48] in which there are 1661 carbon allotropes, confirms the uniqueness of this new carbon allotrope. In addition, the topology analysis is conducted with the help of **https://www.topcryst.com**[49] that reveals it to be a $3,4^4$-c net, which is not included in the reticular chemistry structure resource (RCSR) database.[50]

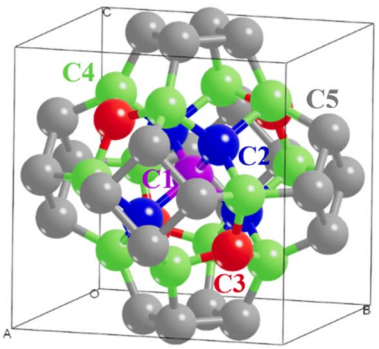

Fig. 1 Crystal structure of AM-C33.

In AM-C33, the C3 atoms are threefold coordinated atoms, which are potentially able to exhibit local magnetic moments.[23,51,52] Here, we investigate the magnetic properties of AM-C33 by setting the initial magnetic moments for C3 atoms. For each sp^2 atom, three spin states are taken into consideration: spin up (U), spin down (D), and non-spin. Hence, there is a total of $3^4 = 81$ different spin configurations. Among those configurations, 9 configurations are independent according to symmetry. After optimization, there are only 5 stable unique configurations, and the crystal information of optimized structures is listed in Table 1. The projected spin density is shown in Fig. S2, and the orbital magnetic moment of different magnetic states is shown in Table S1. The magnetic moment of the p orbital is obviously larger than that of the s orbital, indicating that the p-electron is the main contributor of magnetism in AM-C33. From the table, all the magnetic states are more stable than non-magnetic, and the 2U2D (two spin up and two spin down, hereinafter) anti-ferromagnetic state is the most stable configuration, followed by 3U1D, 4U0D, 1U1D, and 0U0D. The energy of 2U2D is 10.88 meV per atom lower than that of 0U0D. In 2U2D, according to Fig. 1 and S3, the four magnetic atoms are located exactly at the vertices of the tetrahedron. Hence the opposite-spin sublattices are connected by $\bar{4}$ symmetry operation rather than pure inversion or translation, indicating that 2U2D properly exhibits altermagnetism.[10] In addition, the NM state shows the smallest volume, which means that there exists magnetostriction when AM-C33

Table 1 Crystal information of AM-C33 in different magnetic states[a]

Spin configurations	Relative energy to diamond (meV per atom)	Volume (Å^3)	Space group	Lattice constants (Å for length and ° for angles)
NM(0U0D)	557.74	264.134	$P\bar{4}3M$	$a = b = c = 6.4162$
FM(4U0D)	550.97	264.317	$P\bar{4}3M$	$a = b = c = 6.4176$
AFM(2U2D)	546.86	264.193	$P\bar{4}2M$	$a = b = 6.4274$, $c = 6.3951$
FiM(3U1D)	548.09	264.209	$R3M$	$a = b = c = 6.4176$, $\alpha = \beta = \gamma = 89.98$
AFM(1U1D)	551.69	264.222	$CMM2$	$a = b = 6.4080$, $c = 6.4347$, $\gamma = 89.97$

[a] U(D) for spin up (down). After optimization, 1U0D and 2U0D converge to 4U0D and 3U0D (2U1D) converge to 3U1D (2U2D).

transforms from a magnetic state to the non-magnetic state according to zentropy theory.[53,54]

To investigate the stability of AM-C33, the equation of state (EOS) of AM-C33 is calculated, and the results are illustrated in Fig. 2(a). From the figure, AM-C33 is metastable in energy, and each magnetic state is quite robust with pressure: the energy sequence remains as E(2U2D) < E(3U1D) < E(4U0D) < E(1U1D) < E(0U0D) when the lattice constant changes from 96% to 104% of the equilibrium lattice. In addition, the relative energy to the diamond is about 0.547 eV per atom to 0.558 eV per atom, which is lower than that of several previous carbon allotropes, such as P2221-C8 (1.0 eV per atom),[33] T-carbon (1.2 eV per atom)[55] (which was synthesized from experiments[56]), and HM-C21(0.62 eV per atom).[25] The phonon spectrum of AM-C33 in the 2U2D state is shown in Fig. 2(b). There is no imaginary frequency, indicating that AM-C33 is dynamically stable. In addition, the elastic constants for AM-C33 are listed in Table S3, and the Young's modulus is shown in Fig. S4. The elastic constants of each magnetic state satisfy the Born stability criterion, confirming that AM-C33 is mechanically stable. Fig. 2(c) shows the temperature and free energy *vs.* the AIMD step of AM-C33 in the 2U2D state. After 3 ps of AIMD simulation at 300 K, there is no obvious change in the topology of the structure, indicating the thermodynamic stability of AM-C33 at 300 K. In addition, the magnetic moment of AM-C33 at 300 K is shown in Table S2, indicating that the p-electron magnetism still persists at 300 K.

The band structure and density of states (DOS) of AM-C33 with different magnetic states are illustrated in Fig. 3 and S5, respectively. From the figure, AM-C33 exhibits various interesting electronic states. In the NM state, there are three bands across the Fermi surface, and hence there is a peak in the DOS around the Fermi surface. The FM state shows the half-metal characteristics, in which the spin-up channel is a conductor while the spin-down channel is a semiconductor. For the 3U1D state, the VBM shows in the spin-up channel while the CBM occurs in the spin-down channel; hence, it belongs to a bipolar magnetic semiconductor (BMS).[57] The energy degeneracy in momentum space indicates that the 1U1D state is an AFM material. Similar to 1U1D, the 2U2D state is a semiconductor with a bandgap of 0.52 eV. However, the difference is that there exists a clear spin splitting in the M–Γ and A–Z k path in the 2U2D state. Fig. 4 shows the splitting band structure along M–Γ–M′, A′–Γ–A, and A–Z–A′ routes for the 2U2D state. It is obvious that the band structures are symmetrical around the center point between spin up and spin down. In addition, spin symmetry analysis using the amcheck program[58] confirms that the spin symmetry of the 2U2D state complies with the criteria for AM materials,[9] establishing 2U2D as an AM phase. The maximal splitting energy reaches 305.2 meV, which is higher than that of La_2CuO_4,[9] $LaMnO_3$,[59] and κ-Cl.[18] In addition, we calculated several 2 × 1 × 1 supercells with different spin configurations, including seven 4U4D states, five 3U5D states,

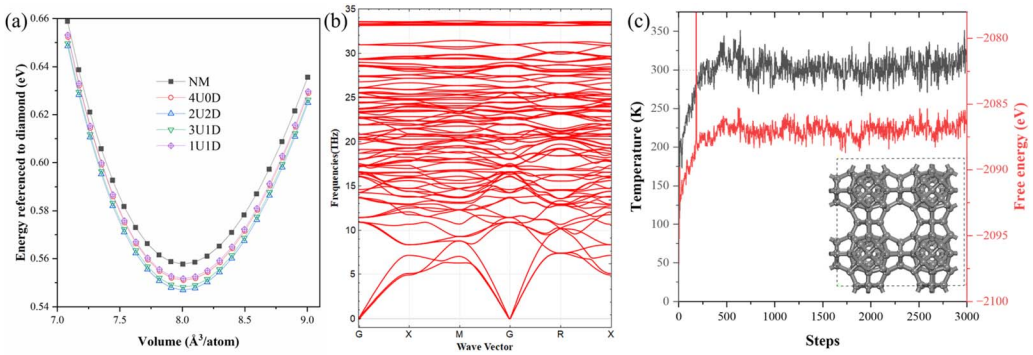

Fig. 2 Stability of AM-C33. (a) Equation of state of AM-C33 with different magnetic states; (b) phonon spectrum of AM-C33 in the 2U2D state; (c) temperature and free energy *vs.* AIMD steps of AM-C33 in the 2U2D state, and the inset at the bottom right corner shows the structure after AIMD simulation.

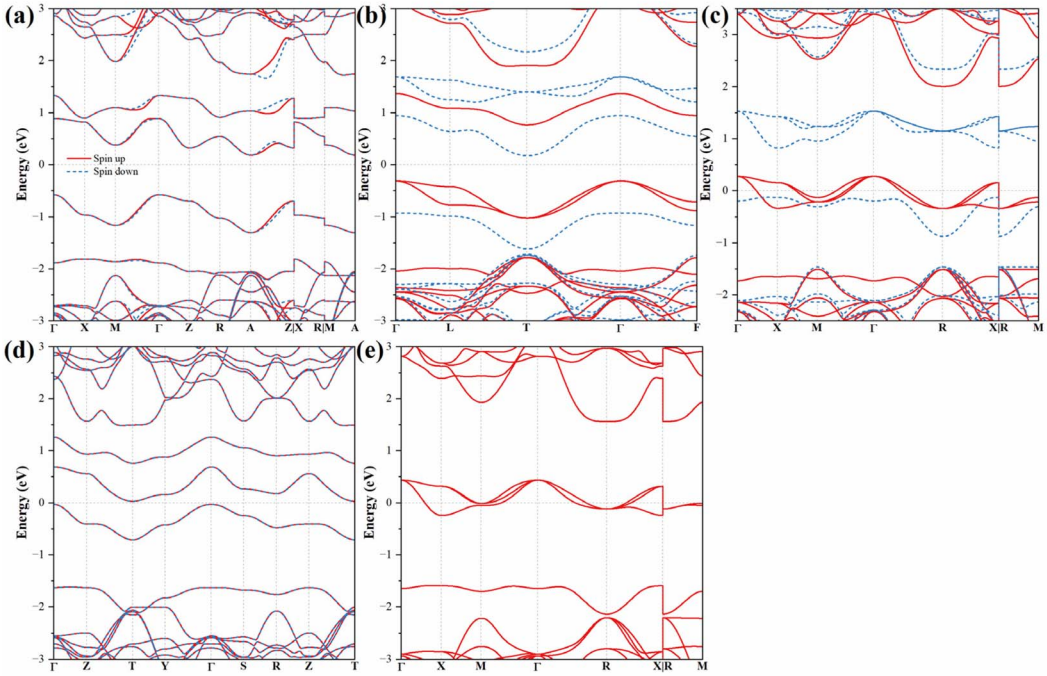

Fig. 3 Band structures of AM-C33. (a) 2U2D; (b) 3U1D; (c) 4U0D; (d) 1U1D; (e) NM.

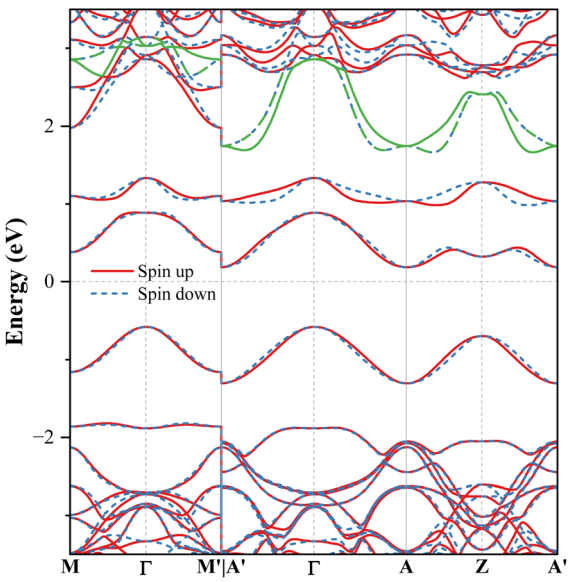

Fig. 4 Band structure of AM-C33 in the 2U2D state along M–Γ–M′, A′–Γ–A, and A–Z–A′. Note: M [0.5, 0.5, 0], M′ [−0.5, 0.5, 0], Γ [0, 0, 0], A′ [−0.5, 0.5, 0.5], A [0.5, 0.5, 0.5], and Z [0, 0, 0.5]. Note: the green lines indicate the band exhibiting maximal spin-splitting energy in each *k*-path.

five 2U6D states, and one 1U7D state. The results are presented in Fig. S7–10 and Table S4. Among these eighteen configurations, the most stable one (labeled 4U4D-5 in Table S4) corresponds to the supercell representation of the 2U2D state. The second most stable configuration (4U4D-2), with an energy difference of only 0.044 meV per atom relative to the 2U2D state, also exhibits an AM character, as illustrated in Fig. S11. Therefore, based on the energy comparisons in Table 1 and Table S4, the ground state of AM-C33 is confirmed to be the AM state. Furthermore, according to the orbital-resolved density of states (Fig. S6), the magnetism is primarily attributed to the p-orbital contributions.

The manipulation of the bandgap and spin-splitting energy magnitude represents a pivotal research frontier in AM semiconductors. Here, we applied external strain (both volumetric and uniaxial) on the AM state, and the results are shown in Fig. 5. With the increase in strain, the CBM of AM-C33 exhibits a negligible shift, while the VBM progressively downshifts toward the Fermi level. Consequently, the bandgap narrows. When the volumetric strain ranges from −5% to +5%, the bandgap decreases from 0.59 eV to 0.38 eV. In contrast, application of uniaxial strain reduces the bandgap more substantially from 0.71 eV to 0.31 eV. Furthermore, the maximal spin-splitting energy exhibits a declining trend with increasing strain. The maximal spin-splitting energy shows in the *k* path of M–Γ–M′ when the strain is less than 1%, and it reaches 347.8 meV and 330.1 meV for volumetric and uniaxial tensile strain, respectively.

The transition temperature is an important parameter for AM materials. The Heisenberg exchange parameters (J_{ij}) for the 2U2D state were calculated (Table S5). The negative value of J_{ij} for the first three nearest neighbors (NNs) indicates that the AFM spin configuration (AM is considered a special case of AFM) is the most stable. The J for the first NN is significantly more negative than those for further neighbors, suggesting that the first NN interactions dominate.[29] Compared to the FM or NM state, the spin symmetry breaking leads to a slight

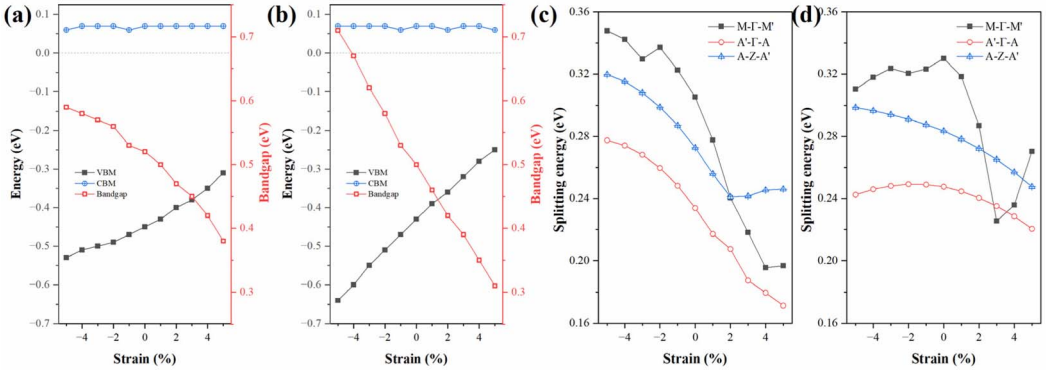

Fig. 5 Effect of strain on band gap and maximal splitting energy in 2U2D. (a) band gap and (b) maximal splitting energy under volumetric strain; (c) band gap and (d) maximal splitting energy under uniaxial tensile strain along the *c* axis.

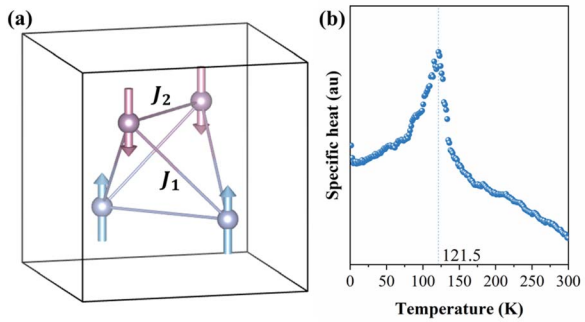

Fig. 6 Specific heat of AM-C33. (a) The interactions in the first NN, and (b) specific heat of AM-C33.

contraction along the *c* axis relative to the *a* and *b* axes. Consequently, two distinct exchange parameters emerged: J_1 (between spin up and spin down sites) and J_2 (between same-spin sites), as illustrated in Fig. 6(a). The larger magnitude of J_1, compared to J_2, further confirms that the magnetic interaction between opposite spins in the 1NN dominates. Based on the full J_{ij} in Table S5, the specific heat was evaluated by Monte Carlo simulation. The result in Fig. 6(b) reveals a magnetic transition temperature of 121.5 K for AM-C33.

4. Conclusion

In conclusion, we designed a novel three-dimensional magnetic carbon, denoted as AM-C33. Its thermodynamic, dynamic, and mechanical stability are rigorously established through first-principles calculations of energy, phonon dispersion spectra, elastic constants, and *ab initio* molecular dynamics. The emergent magnetism originates from threefold coordinated carbon atoms, exhibiting diverse magnetic states, including ferromagnetic (4U0D, half-metal), ferrimagnetic (3U1D, bipolar magnetic semiconductor), and altermagnetic (2U2D) states, and the ground state is altermagnetic. The altermagnetism, which exhibits a transition temperature of 121.5 K, originates from the four-fold inversion symmetry inherent to the opposite-spin sublattice. Furthermore, the bandgap and spin-splitting energy in the altermagnetic phase are tunable by strain engineering. Overall, this work provides a conceptual blueprint for three-dimensional ultralight altermagnetic materials, particularly for advancing carbon-based altermagnetic systems.

Author contributions

Mingqing Liao: conceptualization, project administration, writing – original draft, resources, software, funding acquisition, investigation, methodology, supervision. Yuehua Wang: investigation, data curation, writing – review & editing. Pengcheng Ye: investigation, validation, writing – review & editing. Chenggang Wu: visualization, writing – review & editing. Haoxin Jiang: visualization, writing – review & editing. Fei Zhou: formal analysis, writing – review & editing. Jintong Guan: formal analysis, writing – review & editing. Fengjiang Wang: supervision, writing – review & editing.

Conflicts of interest

There are no conflicts to declare.

Data availability

The data supporting the findings of this study are available within the article and its supplementary information (SI). Supplementary information is available. See DOI: **https://doi.org/10.1039/d5sc05194k**.

Acknowledgements

This work was financially supported by the Jiangsu Province Natural Science Foundation for Youths (No. BK20230673). We gratefully acknowledge HZWTECH for providing computational facilities.

References

1 P. Qin, H. Yan, X. Wang, H. Chen, Z. Meng, J. Dong, M. Zhu, J. Cai, Z. Feng, X. Zhou, L. Liu, T. Zhang, Z. Zeng, J. Zhang, C. Jiang and Z. Liu, *Nature*, 2023, **613**, 485–489.

2 X. Li and J. Yang, *Natl. Sci. Rev.*, 2016, **3**, 365–381.

3 W. Han, R. K. Kawakami, M. Gmitra and J. Fabian, *Nat. Nanotechnol.*, 2014, **9**, 794–807.

4 S. N. Kajale, J. Hanna, K. Jang and D. Sarkar, *Nano Res.*, 2024, **17**, 743–762.

5 T. Jungwirth, X. Marti, P. Wadley and J. Wunderlich, *Nat. Nanotechnol.*, 2016, **11**, 231–241.

6 X. ZHOU, P. QIN and Z. LIU, *Sci. Sin. Phys. Mech. Astron.*, 2026, **56**, 227510.

7 H. Chen, L. Liu, X. Zhou, Z. Meng, X. Wang, Z. Duan, G. Zhao, H. Yan, P. Qin and Z. Liu, *Adv. Mater.*, 2024, **36**, 2310379.

8 C. Song, H. Bai, Z. Zhou, L. Han, H. Reichlova, J. H. Dil, J. Liu, X. Chen and F. Pan, *Nat. Rev. Mater.*, 2025, **10**, 473–485.

9 L. Šmejkal, J. Sinova and T. Jungwirth, *Phys. Rev. X*, 2022, **12**, 031042.

10 L. Šmejkal, J. Sinova and T. Jungwirth, *Phys. Rev. X*, 2022, **12**, 040501.

11 K. Parshukov, R. Wiedmann and A. P. Schnyder, *Phys. Rev. B*, 2025, **111**, 224406.

12 R. D. Gonzalez Betancourt, J. Zubáč, R. Gonzalez-Hernandez, K. Geishendorf, Z. Šobáň, G. Springholz, K. Olejník, L. Šmejkal, J. Sinova, T. Jungwirth, S. T. B. Goennenwein, A. Thomas, H. Reichlová, J. Železný and D. Kriegner, *Phys. Rev. Lett.*, 2023, **130**, 036702.

13 Z. Zhou, X. Cheng, M. Hu, R. Chu, H. Bai, L. Han, J. Liu, F. Pan and C. Song, *Nature*, 2025, **638**, 645–650.

14 X. Jiang, U. Jeong, S. Sato, D. Shin, K. Yabana, B. Yan and N. Park, *ACS Nano*, 2025, **19**(26), 23620–23628.

15 J. Sødequist and T. Olsen, *Appl. Phys. Lett.*, 2024, **124**, 182409.

16 L. Bai, W. Feng, S. Liu, L. Šmejkal, Y. Mokrousov and Y. Yao, *Adv. Funct. Mater.*, 2024, **34**, 2409327.

17 I. Choudhuri, P. Bhauriyal and B. Pathak, *Chem. Mater.*, 2019, **31**, 8260–8285.

18 M. Naka, S. Hayami, H. Kusunose, Y. Yanagi, Y. Motome and H. Seo, *Nat. Commun.*, 2019, **10**, 4305.

19 P.-M. Allemand, K. C. Khemani, A. Koch, F. Wudl, K. Holczer, S. Donovan, G. Grüner and J. D. Thompson, *Science*, 1991, **253**, 301–302.

20 T. L. Makarova, B. Sundqvist, R. Höhne, P. Esquinazi, Y. Kopelevich, P. Scharff, V. A. Davydov, L. S. Kashevarova and A. V. Rakhmanina, *Nature*, 2001, **413**, 716–718.

21 A. L. Sharpe, E. J. Fox, A. W. Barnard, J. Finney, K. Watanabe, T. Taniguchi, M. A. Kastner and D. Goldhaber-Gordon, *Science*, 2019, **365**, 605–608.

22 J. Narayan and A. Bhaumik, *J. Appl. Phys.*, 2015, **118**, 215303.

23 Y. Sakai, J. R. Chelikowsky and M. L. Cohen, *Phys. Rev. Mater.*, 2018, **2**, 074403.

24 Y. Zhang, S. Talapatra, S. Kar, R. Vajtai, S. K. Nayak and P. M. Ajayan, *Phys. Rev. Lett.*, 2007, **99**, 107201.

25 J. Zhao, M. Liao, J. Zhang, Y. Wang, C. Wu, H. Jiang, F. Zhou, J. Guan, D. Yang, N. Qu and F. Wang, *Appl. Phys. Lett.*, 2025, **126**, 162402.

26 H.-B. Li and Z.-G. Shao, *Phys. Rev. B*, 2025, **111**, 214420.

27 B. Viña-Bausá, M. A. García-Blázquez, S. Chourasia, R. Carrasco, D. Expósito, I. Brihuega and J. J. Palacios, *Nano Lett.*, 2025, **25**, 11554–11561, DOI: **10.1021/acs.nanolett.5c02091**.

28 Y. Che, H. Lv, X. Wu and J. Yang, *Chem. Sci.*, 2024, **15**, 13853–13863.

29 Y. Che, H. Lv, X. Wu and J. Yang, *J. Am. Chem. Soc.*, 2025, **147**, 14806–14814.

30 Y. Che, Y. Chen, X. Liu, H. Lv, X. Wu and J. Yang, *JACS Au*, 2025, **5**, 381–387.

31 X. Shi, C. He, C. J. Pickard, C. Tang and J. Zhong, *Phys. Rev. B*, 2018, **97**, 014104.

32 M. Liao, J. Maimaitimusha, X. Zhang, J. Zhu and F. Wang, *Front. Phys.*, 2022, **17**, 63507.

33 M. Liao, F. Wang, J. Zhu, Z. Lai and Y. Liu, *Scr. Mater.*, 2022, **212**, 114549.

34 P. E. Blöchl, *Phys. Rev. B*, 1994, **50**, 17953–17979.

35 Hongzhiwei Technology, Device Studio, Version 2023A, **https://cloud.hzwtech.com/web/product-service?id=6**, (accessed 12 October 2024).

36 J. P. Perdew, K. Burke and M. Ernzerhof, *Phys. Rev. Lett.*, 1996, **77**, 3865–3868.

37 H. J. Monkhorst and J. D. Pack, *Phys. Rev. B*, 1976, **13**, 5188–5192.

38 M. Cococcioni and S. de Gironcoli, *Phys. Rev. B: Condens. Matter Mater. Phys.*, 2005, **71**, 035105.

39 P. Giannozzi, S. de Gironcoli, P. Pavone and S. Baroni, *Phys. Rev. B*, 1991, **43**, 7231–7242.

40 M. Liao, Y. Liu, S.-L. Shang, F. Zhou, N. Qu, Y. Chen, Z. Lai, Z.-K. Liu and J. Zhu, *Comput. Phys. Commun.*, 2021, **261**, 107777.

41 M. Liao, Y. Liu, F. Zhou, T. Han, D. Yang, N. Qu and Z. Lai, *Comput. Phys. Commun.*, 2022, **280**, 108478.

42 M. Liao, Y. Liu, P. Cui, N. Qu, F. Zhou, D. Yang, T. Han, Z. Lai and J. Zhu, *Comput. Mater. Sci.*, 2020, **172**, 109289.

43 X. He, N. Helbig, M. J. Verstraete and E. Bousquet, *Comput. Phys. Commun.*, 2021, **264**, 107938.

44 W. Zhou, D. Zheng, Q. Liu, D. Lu, Y. Liu, P. Lin, Y. Huang, X. Peng, J. J. Bao, C. Cai, Z. Jin, J. Wu, H. Zhang, G. Jin, Y. Ji, Z. Shen, X. Liu, L. Sun, Y. Cao, M. Sun, J. Liu, T. Chen, R. Liu, Y. Li, H. Han, X. Liang, T. Bao, N. Chen, H. Ren, X. Zhang, Z. Liu, Y. Fu, M. Liu, Z. Li, T. Wen, Z. Tang, Y. Xu, W. Duan, X. Wang, Q. Gu, F.-Z. Dai, Q. Zheng, J. Zhao, Y. Zhang, Q. Ou, H. Jiang, S. Liu, B. Xu, S. Xu, X. Ren, L. He, L. Zhang and M. Chen, *arXiv*, 2025, arXiv:2501.08697, DOI: **10.48550/arXiv.2501.08697**.

45 P. Li, X. Liu, M. Chen, P. Lin, X. Ren, L. Lin, C. Yang and L. He, *Comput. Mater. Sci.*, 2016, **112**, 503–517.

46 J. D. Alzate-Cardona, D. Sabogal-Suárez, R. F. L. Evans and E. Restrepo-Parra, *J. Phys. Condens. Matter*, 2019, **31**, 095802.

47 R. F. L. Evans, W. J. Fan, P. Chureemart, T. A. Ostler, M. O. A. Ellis and R. W. Chantrell, *J. Phys. Condens. Matter*, 2014, **26**, 103202.

48 R. Hoffmann, A. A. Kabanov, A. A. Golov and D. M. Proserpio, *Angew. Chemie Int. Ed.*, 2016, **55**, 10962–10976.
49 V. A. Blatov, A. P. Shevchenko and D. M. Proserpio, *Cryst. Growth Des.*, 2014, **14**, 3576–3586.
50 M. O'Keeffe, M. A. Peskov, S. J. Ramsden and O. M. Yaghi, *Acc. Chem. Res.*, 2008, **41**, 1782–1789.
51 Y. Aierken, O. Leenaerts and F. M. Peeters, *Phys. Rev. B*, 2016, **94**, 155410.
52 Z. Lai and X. Zhu, *Solid State Commun.*, 2019, **302**, 113707.
53 Z.-K. Liu, Y. Wang, S.-L. Shang and J. Phase, *Equilibria Diffus*, 2022, **43**, 598–605.
54 M. Liao, W. Y. Wang, Y. Wang, S.-L. Shang and Z.-K. Liu, *Acta Metall. Sin.*, 2024, **60**, 1379–1387.
55 X.-L. Sheng, Q.-B. Yan, F. Ye, Q.-R. Zheng and G. Su, *Phys. Rev. Lett.*, 2011, **106**, 155703.
56 J. Zhang, R. Wang, X. Zhu, A. Pan, C. Han, X. Li, D. Zhao, C. Ma, W. Wang, H. Su and C. Niu, *Nat. Commun.*, 2017, **8**, 683.
57 J. Li, X. Li and J. Yang, *Fundam. Res.*, 2022, **2**, 511–521.
58 A. Smolyanyuk, L. Šmejkal and I. I. Mazin, *SciPost Phys. Codebases*, 2024, **30**, 30.
59 L.-D. Yuan, Z. Wang, J.-W. Luo and A. Zunger, *Phys. Rev. Mater.*, 2021, **5**, 014409.